ACS Catalysis

Research Article

pubs.acs.org/acscatalysis

Ex Situ and Operando Studies on the Role of Copper in Cu-Promoted SiO_2–MgO Catalysts for the Lebedev Ethanol-to-Butadiene Process

Carlo Angelici,[†] Florian Meirer,[†] Ad M. J. van der Eerden,[†] Herrick L. Schaink,[†] Andrey Goryachev,[‡] Jan P. Hofmann,[‡] Emiel J. M. Hensen,[‡] Bert M. Weckhuysen,*[,†] and Pieter C. A. Bruijnincx*[,†]

[†]Inorganic Chemistry and Catalysis, Debye Institute for Nanomaterials Science, Utrecht University, Universiteitsweg 99, 3584 CG Utrecht, The Netherlands

[‡]Laboratory of Inorganic Materials Chemistry, Schuit Institute of Catalysis, Department of Chemical Engineering and Chemistry, Eindhoven University of Technology, P.O. Box 513, 5600 MB Eindhoven, The Netherlands

Supporting Information

ABSTRACT: Dehydrogenation promoters greatly enhance the performance of SiO_2–MgO catalysts in the Lebedev process. Here, the effect of preparation method and order of addition of Cu on the structure and performance of Cu-promoted SiO_2–MgO materials is detailed. Addition of Cu to MgO via incipient wetness impregnation (IWI) or coprecipitation (CP) prior to wet-kneading with SiO_2 gave similar butadiene yields (~40%) as when Cu was added to the already wet-kneaded catalyst. In contrast, the catalyst prepared by impregnation of Cu on SiO_2 first proved to be the worst catalyst of the series. TEM, XRD, and XPS analyses suggested that, for all catalyst materials, Cu^{2+} forms a solid solution with MgO. This was confirmed by UV–vis, XANES, and EXAFS data, with Cu being found in a distorted octahedral geometry. As a result, the acid–base properties, as determined by Pyridine- and $CDCl_3$–IR as well as NH_3-TPD, are modified, contributing to the improved performance. Operando XANES and EXAFS studies of the evolution of the copper species showed that Cu^{2+}, the only species initially present, is extensively reduced to a mixture of Cu^0 and Cu^+, leaving only a limited amount of unreduced Cu^{2+}. This formation of Cu^0 is the result of the reducing environment of the Lebedev process and is thought to be mainly responsible for the improved performance of the Cu-promoted catalysts.

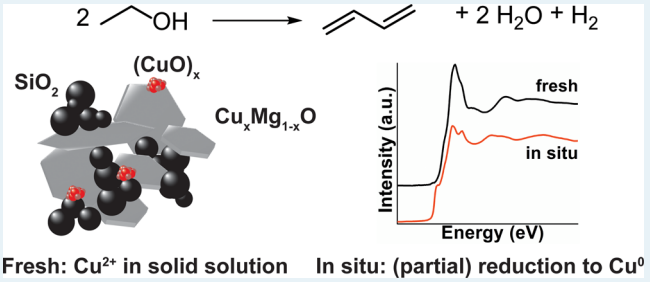

KEYWORDS: *ethanol, operando, solid solution, SiO_2–MgO catalysts, butadiene*

1. INTRODUCTION

SiO_2–MgO materials have been extensively explored for the ethanol-to-butadiene Lebedev process.[1,2] The performance of these catalysts can be greatly enhanced by the addition of a third component, typically a transition metal or metal oxide. These promoters generally improved butadiene yields, by increasing the amount of acetaldehyde produced via ethanol dehydrogenation.[3] The addition of Cr,[3,4] Ni,[5] Zn,[3] Cu[3] oxides and metallic Ag[6] has, for example, been studied in this respect. That addition of such metal oxides is not always beneficial was shown by Natta and Rigamonti, who prepared ZnO- and CuO-promoted SiO_2–MgO materials by coprecipitation (CP) of the carbonates of Mg with Zn and Cu, respectively.[3] The reduced performance shown by these catalysts was attributed to the formation of an $M_xMg_{1-x}O$ solid solution (with M = Cu or Zn), resulting in reduced dehydrogenation and condensation activity. No experimental evidence for this proposed structure–activity relation was reported, however. Moreover, Makshina et al. showed that simultaneous impregnation of Zn and Mg nitrates on SiO_2 resulted in a catalyst giving a lower butadiene yield than one synthesized by adding $Zn(NO_3)_2$ to a SiO_2–MgO material that was obtained by a wet-kneading procedure;[6] again, this was tentatively attributed to the formation of mixed Zn, Mg silicates. The latter example furthermore emphasizes the importance of preparation method and order of component addition, when using transition metal oxides to promote the activity of SiO_2–MgO catalysts. Finally, Kitayama et al. also proposed NiO on SiO_2–MgO materials to actually consist of mixed Ni, Mg silicates and Ni dispersed in MgO.[5] In their case, the formation of such a mixed metal silicate was in fact considered one of the prime reasons for its good catalytic activity.

Parameters such as promoter oxidation state, loading and order of addition, will all affect the final catalyst structure and can thus be optimized with regard to their effect on catalytic performance. Indeed, as illustrated below and suggested before, promotion of these MgO-containing materials will affect the acid–base properties of the catalysts,[7] the balance of which is key to butadiene production. Studies on these dehydrogenation promoters typically report limited characterization data on both

Received: April 10, 2015
Revised: August 23, 2015
Published: September 9, 2015

DOI: 10.1021/acscatal.5b00755
ACS Catal. 2015, 5, 6005–6015

Table 1. Overview of the Different Preparation Methods for the Various Catalyst Materials Studied Here for the Lebedev Ethanol-to-Butadiene Process

sample name	first step	second step
CuO/SiO_2–MgO (III)	WK SiO_2, MgO	IWI $Cu(NO_3)_2$ on SiO_2–MgO (III)
CuO/SiO_2	IWI $Cu(NO_3)_2$ on SiO_2	-[a]
CuO/MgO	IWI $Cu(NO_3)_2$ on MgO	-[a]
CuO/SiO_2(IWI)+MgO	IWI $Cu(NO_3)_2$ on SiO_2	WK with $Mg(OH)_2$
CuO/MgO(IWI)+SiO_2	IWI $Cu(NO_3)_2$ on $Mg(OH)_2$	WK with SiO_2
CuO/MgO(CP)+SiO_2	CP $Cu(NO_3)_2$, $Mg(NO_3)_2$	WK with SiO_2

[a]Not applicable. WK, wet-kneading; IWI, incipient wetness impregnation; CP, coprecipitation.

the acid–base and structural properties, making the explanations for the observed beneficial or detrimental catalytic effects often somewhat speculative.

We previously showed that the performance of wet-kneaded SiO_2–MgO catalysts could be significantly improved by the addition of CuO (1 wt %) via incipient wetness impregnation (IWI, Figure S1A), followed by calcination in stagnant air.[8] As Cu-promotion resulted in a significantly increased acetaldehyde yield, it was proposed that upon addition of Cu the aldol condensation (see Scheme S2 for the commonly accepted mechanism) rather than acetaldehyde formation becomes rate-determining. On the basis of the drop in ethylene and diethyl ether also observed upon Cu promotion, we also proposed copper to poison the most acidic sites of the SiO_2–MgO materials. UV–vis results provided some insight into how the type of Cu species present depended on preparation and correlated with catalyst performance.[8] In addition to isolated CuO species supported on either SiO_2 or MgO,[9−15] subnanometric cluster-like $(CuO)_x$ species were, for example, identified, and the extent of their presence was found to coincide with improvements in butadiene yield[16] (Figure S1); these $(CuO)_x$ clusters were suggested to enhance the rate-determining acetaldehyde condensation step.[17,18] Transmission electron microscopy (TEM) showed the morphology of wet kneaded SiO_2–MgO materials not to be modified upon subsequent Cu-promotion,[8] nor were any copper nanoparticles (NP) detected. Energy-dispersive X-ray spectroscopy (EDX) did show that Cu is present on both Si- and Mg-rich phases of the samples, however.[8] Although TEM is often used to study Cu(O) NP on SiO_2[19−22] and metallic copper on MgO,[23−25] reports on TEM imaging of CuO/MgO samples are very limited. This might be due to lack of contrast between CuO and MgO or, alternatively, to a very high CuO dispersion.[26] El-Shobaky et al., for instance, did not observe any CuO reflections by X-ray diffraction (XRD) for CuO/MgO with up to 23 wt % of copper oxide,[27] concluding that a solid solution is formed for samples treated at 673 K (our samples were calcined at 773 K, see below). Other have also observed the formation of $Cu_xMg_{1-x}O$ solid solutions.[28,29] For our materials, XRD analysis also did not show any CuO reflections, perhaps because of low loading or as a result of solid solution formation. Grirrane et al. suggested that CuO NP can be formed on MgO and visualized these structures with TEM.[30] While the NP are difficult to identify in the TEM images, their formation might be due to the particular low-temperature preparation method used, in which solid solution formation might be prevented. Finally, Ueda et al. proposed that the insertion of transition metal cations with a slightly larger ionic radius than Mg^{2+}, e.g., Cu^{2+} (0.65 and 0.69 Å, respectively),[31] in MgO increases its basicity.[7] This was thought to be the reason for the improved activity and selectivity shown by Cu-containing MgO over MgO in the dehydrogenation of 2-propanol. Cu promotion can thus be expected to affect the performance of Lebedev catalysts not only by introducing a redox functionality that aids in acetaldehyde formation but also by modifying their acid–base properties.

Knowledge of the structural and morphological properties of Cu in CuO/SiO_2–MgO catalysts is thus still very limited.[32,33] More insight into the nature, dispersion, and role of CuO, and in fact metal oxide promoters in general, in the catalysts for the Lebedev process is therefore highly desired. Furthermore, it is essential to get insight into any evolution in the nature of the metal (oxide) promoter under Lebedev reaction conditions; this has not, however, been studied yet. Indeed, given the reducing environment of the ethanol-to-butadiene process, changes in oxidation state of transition metal oxides might be expected. Ethanol, for instance, is able to reduce both noble[34] and non-noble transition metal oxides,[35] with CuO reduction by ethanol having been reported at temperatures of ≥453 K (i.e., significantly lower than our reaction temperature of 698 K).[36] H_2 is furthermore formed during reaction and could also cause reduction of CuO. The observation that SiO_2–MgO materials promoted with NiO, ZnO, CuO, or metallic Ag all performed remarkably similarly in catalysis[6] suggests that similar species might be formed under reaction conditions.

Different materials were synthesized with the expectation that the order of component addition will impact catalyst performance by altering the location and nature of Cu species formed, the (extent of) solid solution formation, and the acid/base properties of the materials. To this extent, catalysts prepared supporting Cu on either SiO_2 or MgO prior to the addition of the other component during wet-kneading are compared with a sample synthesized by incipient wetness impregnation (IWI) of copper on already wet-kneaded SiO_2–MgO (CuO/SiO_2–MgO (III)). The as-synthesized materials were extensively characterized with Fourier transform infrared spectroscopy after pyridine and deuterated chloroform adsorption (Pyridine– and $CDCl_3$–IR), temperature-programmed desorption of ammonia (NH_3–TPD), TEM, XRD, UV–vis, and X-ray photoelectron spectroscopy (XPS), X-ray absorption near edge structure (XANES), and extended X-ray absorption fine structure (EXAFS) analyses. These techniques provided information into the speciation, oxidation state, and geometry of Cu species in the various samples and into changes in the acid/base properties upon copper addition. The results show that the order of addition indeed affects the presence of $(CuO)_x$ clusters and thus catalyst performance.[8] In addition, a large portion of copper was found to be present in a $Cu_xMg_{1-x}O$ solid solution, which again affects the acid–base properties. Furthermore, one selected CuO/SiO_2–MgO catalyst was studied with X-ray Absorption Spectroscopy (XAS) under operando conditions to investigate the nature

DOI: 10.1021/acscatal.5b00755
ACS Catal. 2015, 5, 6005−6015

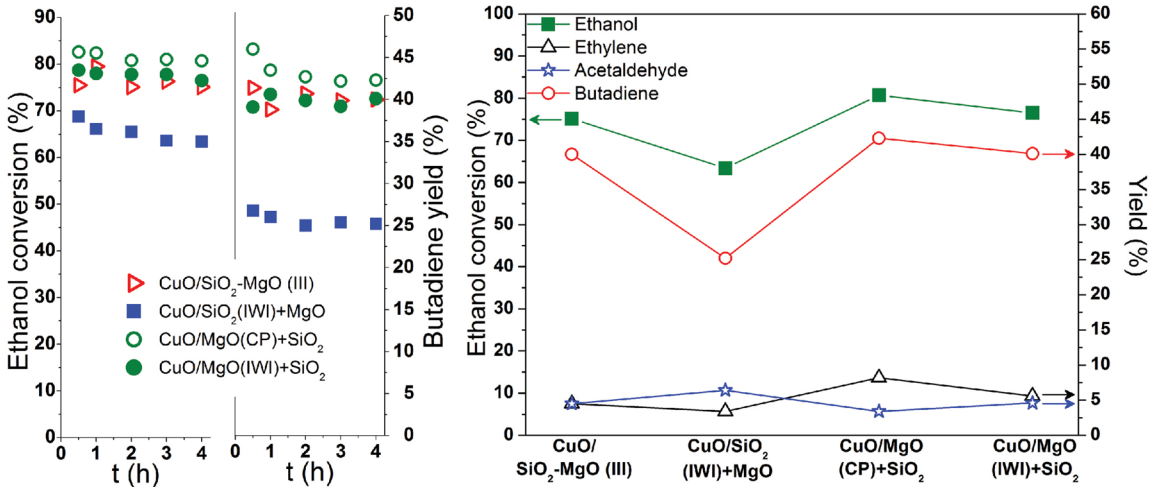

Figure 1. Ethanol conversion (left), butadiene yield (middle), and conversion and yield of the main (by-) products for CuO/SiO_2–MgO (III) and the catalyst materials prepared varying the order of addition of CuO.

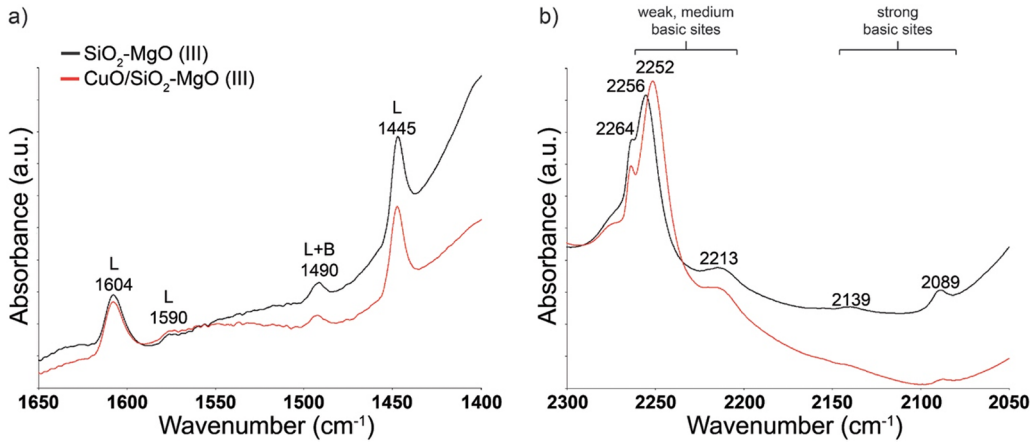

Figure 2. (a) Pyridine-IR spectra at 423 K in the region 1650–1400 cm^{-1} and (b) $CDCl_3$–IR spectra at 323 K in the region 2300–2050 cm^{-1} for SiO_2–MgO (III) and CuO/SiO_2–MgO (III).

of the active copper species during ethanol-to-butadiene conversion. This way, it could be shown that the reducing atmosphere of the Lebedev process indeed causes reduction of the Cu^{2+} species originally found in the $Cu_xMg_{1-x}O$ solid solution to a mixture of unreduced Cu^{2+}, Cu^+ and large amounts of metallic copper, the latter of which is held responsible for the improved ethanol dehydrogenation activity.

2. RESULTS AND DISCUSSION

2.1. Performance of the Catalysts. To study the effect of copper addition order, $Cu(NO_3)_2$ was supported on either SiO_2 or MgO *prior to* wet-kneading with the other oxide and performance compared to the benchmark CuO/SiO_2–MgO (III) catalyst, prepared by copper addition *after* wet-kneading. CuO/SiO_2(IWI)+MgO was thus prepared by supporting copper on SiO_2 by IWI, before wet-kneading with $Mg(OH)_2$ (Table 1). Two other samples were prepared by adding CuO to MgO with two different techniques: $CuO/MgO(IWI)+SiO_2$ was prepared by supporting $Cu(NO_3)_2$ on $Mg(OH)_2$ via IWI, while for $CuO/MgO(CP)+SiO_2$, $Cu(NO_3)_2$ and $Mg(NO_3)_2$ were coprecipitated with TMAOH; in both cases, the resulting solid was then wet-kneaded with SiO_2. Lastly, all catalysts were calcined in stagnant air at 773 K for 5 h (see Supporting Information (SI) for experimental details).

Ethanol conversions, determined at 698 K for 4 h time on stream (Figure 1), are quite similar for all catalysts, with the exception of CuO/SiO_2(IWI)+MgO, which proved less active. The latter sample also gave a significantly lower butadiene yield, showing that deposition of copper on silica first is undesired. Overall, quite similar product distributions (see the SI for a full description of products observed) were obtained with very small variations in acetaldehyde formation and a slightly higher ethylene yield for $CuO/MgO(CP)+SiO_2$.

CuO/SiO_2 and CuO/MgO, prepared as reference samples for the characterization studies, both showed much lower ethanol conversion levels (Figure S2) with no or very little (1%) butadiene formation, respectively. Moreover, CuO/SiO_2 showed the highest amount of acetaldehyde, confirming that MgO or MgO-containing catalysts are required for the aldol condensation step in the mechanism. Previously, NiO/SiO_2 and NiO/MgO were also found to be essentially inactive toward butadiene formation.[5] These results further support the notion that both components are required, with the presence of both MgO and the magnesium silicates that formed upon wet-kneading being essential for catalysis,[37] also in the case of Cu-promoted materials.

2.2. Acid–Base Properties of the Catalysts. Different characterization techniques were used to compare the acid–

DOI: 10.1021/acscatal.5b00755
ACS Catal. 2015, 5, 6005–6015

base properties of one selected Cu-containing sample, i.e., CuO/SiO_2–MgO (III), with the corresponding, unpromoted material. Pyridine-IR results reported in Figure 2a show that only Lewis acid sites are present in both materials;[38] Larina et al., on the other hand, recently reported both Lewis and Brønsted acid sites to be present on SiO_2–MgO catalysts, prior and after promotion with ZnO.[39] Although the similar intensities observed by Pyridine-IR suggest similar amounts of acidic sites, NH_3-TPD shows the Cu-promoted sample to have less acidic sites (Table 2). We previously already observed a similar discrepancy between these techniques and attributed this to the difference in probe molecule size, with NH_3 able to probe a higher and more realistic amount of acidic sites.[40] The results thus show that some acidic sites of the original SiO_2–MgO material are poisoned upon Cu addition.

Table 2. Amount of Acidic Sites Obtained by NH_3-TPD Analysis, Butadiene and Ethylene Yields for SiO_2–MgO (III) and CuO/SiO_2–MgO (III)

sample	number of acidic sites (mmol g^{-1})	butadiene yield (%)	ethylene yield (%)
SiO_2–MgO (III)	0.219	16	12
CuO/SiO_2–MgO (III)	0.180	37	4

Figure 2b shows the remarkable differences between basic sites found on the promoted and unpromoted SiO_2–MgO (III) as probed by $CDCl_3$–IR (see ref 40 for detailed assignments). In particular, the FT-IR peak due to weak basic sites shifted to lower wavenumbers for the Cu-containing sample (i.e., from 2256 to 2252 cm^{-1}); such a shift indicates that the relative strength of these sites is higher in CuO/SiO_2–MgO (III).[41] Moreover, a slightly larger amount of weak basic sites is seen for the promoted sample.

The increase in amount and relative strength of weak basic sites might be the result of solid solution formation between CuO and MgO, as discussed below. It is indeed in line with the proposal by Ueda et al. that solid solution formation causes a distortion in the MgO crystal lattice resulting in increased basicity.[7] The FT-IR peak assigned to medium basic sites at 2213 cm^{-1} is similar in both position and intensity in the two samples. The intensity of the two FT-IR peaks assigned to strong basic sites of the Mg–O(H)-Si type,[40] i.e., those at ~2139 and 2089 cm^{-1}, is significantly lower for the CuO/SiO_2–MgO (III) sample, however. This suggests copper addition to also poison the strong basic sites in the Cu-containing material.

The much lower yields of ethylene generally seen upon Cu-promotion (Table 2),[8] are in line with the lower amount of acidic and strong basic sites observed for CuO/SiO_2–MgO (III). The significantly higher butadiene yield observed for the promoted sample might be not only the result of the dehydrogenation activity of Cu but also the result of the increase in relative strength and amount of weak basic sites that are beneficial for the aldol condensation step. To better understand the reasons behind the modified acid–base properties and the effect of the different preparation on the nature of Cu species, the set of samples was extensively characterized, as detailed below.

2.3. Catalyst Morphology, Structure, and Copper Geometry. Figure 3 shows the TEM images of CuO/SiO_2–MgO (III), CuO/MgO and CuO/SiO_2. No copper species can be seen on CuO/MgO and CuO/SiO_2–MgO (III). On the contrary, well-defined, quite monodisperse (~2–3 nm) CuO NP are present on CuO/SiO_2.

XRD analyses (Figure 4) show that the intensity of the peaks associated with the crystalline periclase MgO phase varies for the MgO-containing samples. For all wet-kneaded samples, the broadening (with reference to CuO/MgO) and reduced intensity suggests significant chemical changes in the MgO component. Moreover, the two low-intensity peaks at ~41 and 45 2θ degrees seen for CuO/SiO_2 and assigned to a tenorite

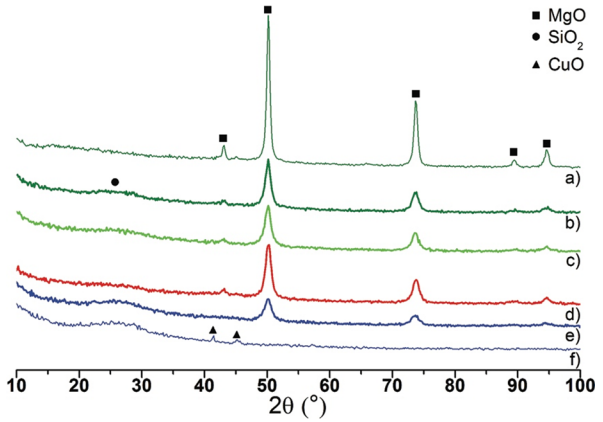

Figure 4. XRD patterns of (a) CuO/MgO, (b) CuO/MgO-(IWI)+SiO_2, (c) CuO/MgO(CP)+SiO_2, (d) CuO/SiO_2–MgO (III), (e) CuO/SiO_2(IWI)+MgO, and (f) CuO/SiO_2.

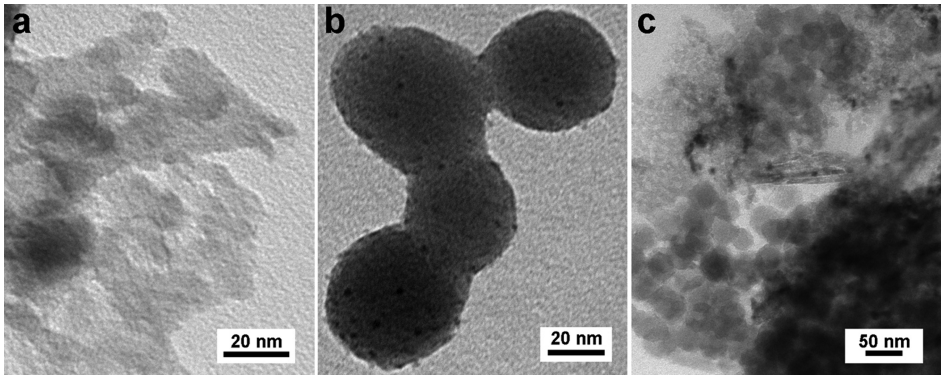

Figure 3. TEM images of (a) CuO/MgO, (b) CuO/SiO_2, and (c) CuO/SiO_2–MgO (III).

DOI: 10.1021/acscatal.5b00755
ACS Catal. 2015, 5, 6005–6015

phase,[42] i.e., crystalline CuO NP, show that they can indeed be detected with XRD even at these low Cu loadings of 1 wt %. It is therefore telling that all MgO-containing samples show no such peaks; given that all materials were thermally treated in the same way, this clearly shows that the reason CuO is not seen by TEM in the other samples is not because of lack of contrast, but is rather the consequence of improved copper dispersion.

The UV−vis spectra of these materials proved quite complex, with a number of features contributing to the observed intensity (Figure 5). For the CuO/SiO_2 material, a very broad d−d

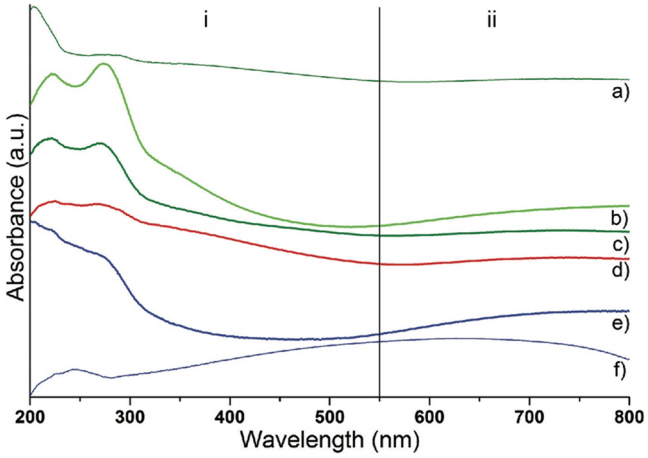

Figure 5. UV−vis spectra of (a) CuO/MgO, (b) CuO/MgO-(CP)+SiO_2, (c) CuO/MgO(IWI)+SiO_2, (d) CuO/SiO_2−MgO (III), (e) CuO/SiO_2(IWI)+MgO, and (f) CuO/SiO_2. The spectra are offset for clarity. i, bands assigned to LMCT transitions; ii, bands assigned to d−d transitions.

transition is detected at ∼625 nm, well in line with the 636 nm reported for bulk CuO (see Figure S3).[43,44] The UV−vis spectra of all ternary oxides and CuO/MgO are, however, very different, suggesting copper not to be in the square planar geometry of (bulk) CuO. Indeed, the absorption bands observed in the 200−300 nm region can be assigned to ligand-to-metal charge transfer (LMCT) bands of isolated CuO species on different supports.[9,10,15] For example, Bravo-Suárez et al. attributed a band at ∼260 nm detected for $CuMgAlO_x$ to an LMCT of Cu^{2+} in an octahedral field.[16] Moreover, the d−d transitions seen at 700−800 nm are also indicative of Cu^{2+} species in a (distorted) octahedral field.

The 300−500 nm absorption band, previously assigned to LMCT transitions of subnanometric $(CuO)_x$ clusters,[10,11,16] has a similar intensity for the three catalyst materials that show a similar, superior performance, i.e., CuO/MgO(CP)+SiO_2, CuO/MgO(IWI)+SiO_2 and CuO/SiO_2−MgO (III); the same feature is also observed in CuO/MgO. On the other hand, for the worst catalyst, CuO/SiO_2(IWI)+MgO, the 300−500 nm absorption band is negligible in intensity. With this shoulder also being absent in CuO/SiO_2, this means that the formation of small $(CuO)_x$ clusters is favorable on MgO-containing materials but not on SiO_2.

TEM and XRD results thus show CuO NP to be present on CuO/SiO_2 but not on any of the MgO-containing materials. Moreover, the UV−vis results suggest the copper species in all MgO-containing samples to have a (distorted) octahedral geometry. All of this points at solid solution formation with the Cu^{2+} atoms being located at crystal lattice sites of MgO. XPS, XANES, and EXAFS analyses, discussed below, further confirm this and provide additional insight into nature, oxidation state and geometry of Cu species in the various samples.

A selected number of samples were studied with XPS and binding energies (BE) of the Cu $2p_{3/2}$, Si 2p and Mg 2p signals are reported in Table 3. In line with the TEM, XRD, and UV−vis results, the BE of in CuO/SiO_2 is in good agreement with the one observed for pure SiO_2.[45] Interestingly, the Si 2p values for the CuO/SiO_2−MgO samples are significantly lower, however, and correspond well to the range Si 2p BE reported for a number of (magnesium) silicates by Okada et al.[46] The BE of Si 2p of 102.6 eV reported for talc (a magnesium silicate that can be formed upon wet-kneading of SiO_2 and MgO)[37] is similar to the BE of Si observed for the various CuO/SiO_2−MgO samples.

Table 3. Binding Energies of Cu $2p_{3/2}$, Si 2p, and Mg 2p Levels in the Various Samples

sample	Cu $2p_{3/2}$ BE (eV)	Si 2p BE (eV)	Mg 2p BE (eV)
CuO/SiO_2	934.8	104.2	-[a]
CuO/MgO	933.5	-[a]	49.7
CuO/SiO_2−MgO (III)	934.0	102.8	50.3
CuO/SiO_2(IWI)+MgO	933.9	103.0	50.0
CuO/MgO(IWI)+SiO_2	933.7	102.5	49.8

[a]The element is not present in the analyzed sample.

The XPS data also showed all copper to be Cu^{2+} in all samples, based on the characteristic shakeup satellite peaks[47] at approximately 943 eV alongside a BE of the Cu $2p_{3/2}$ core level (Table 3) in the range of 933−935 eV; indeed, the BE of bulk CuO is reported in the range of 933.2−934.2 eV,[48,49] whereas Cu^0 and Cu^+ species are generally found at ∼932.0−932.5 eV.[50] The low amount of Cu detected at the surface of all MgO-containing samples hinders the deconvolution of the signal for Cu $2p_{3/2}$ into contributions of different copper species. The Cu $2p_{3/2}$ region can thus only be used for semiquantitative analysis of Cu abundance and to assess the variation in BE position among the different samples. Moreover, the high-resolution Cu $2p_{3/2}$ spectra (Figure S4) show the surface Cu amounts to vary widely, being the highest on CuO/SiO_2. For CuO/MgO, it is below the quantification limit, which implies that the copper must be distributed throughout the bulk of the sample (see UV−vis and XAS below). Indeed, this provides further evidence for solid solution formation and inclusion of copper in the crystal lattice of MgO. Finally, for all CuO/SiO_2−MgO samples a surface copper amount intermediate between that of CuO/SiO_2 and that of CuO/MgO was observed; this might be due to Cu being present on both oxides, as well as on the magnesium silicates formed during wet-kneading. The BE of Cu $2p_{3/2}$ was observed to vary as well and follows the order: CuO/SiO_2 > CuO/SiO_2−MgO (III) ≈ CuO/SiO_2(IWI)+MgO ≈ CuO/MgO(IWI)+SiO_2 > CuO/MgO. Bennici et al. proposed shifts to higher binding energy to correlate with the acidity of the support for CuO supported on SiO_2−Al_2O_3.[47] In our case, the order listed above also seems to be in line with the overall acidity/basicity of the supports.

Ex situ XAS analysis provided further information on Cu speciation, coordination, and chemical environment in the as-synthesized samples. The XANES spectra show two pre-edge features (labeled 1 and 2 in Figure 6). This feature at ∼8979 eV, originating from the dipole forbidden 1s → 3d transition, is considered a signature for Cu^{2+} species.[51] This, together with

DOI: 10.1021/acscatal.5b00755
ACS Catal. 2015, 5, 6005−6015

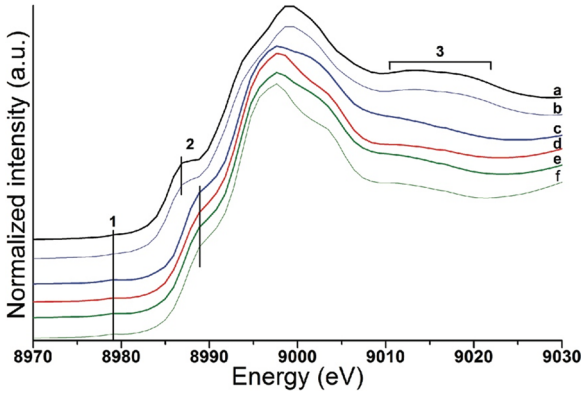

Figure 6. Normalized XANES spectra of (a) CuO, (b) CuO/SiO_2, (c) CuO/SiO_2(IWI)+MgO, (d) CuO/SiO_2–MgO (III), (e) CuO/MgO(IWI)+SiO_2, and (f) CuO/MgO.

the absence of a feature at 8982 eV characteristic of Cu^+ confirms all copper to be present as Cu^{2+} in all samples. Pre-edge feature 2, due to a 1s → 4p transition, is again characteristic of Cu^{2+}.[52] The position of this feature depends on local copper symmetry, in addition to its charge.[53] Feature 2 is centered at ∼8987 eV for CuO and CuO/SiO_2, implying it to be very similar to bulk CuO (as confirmed by EXAFS analyses, see below). Cu^{2+} in tenorite has been described as square planar (i.e., with four oxygen atoms at ∼1.95 Å),[54] but can also be considered as strongly distorted octahedral when taking into account the two oxygen atoms at 2.78 Å (see Table S2). Notably, feature 2 is found at a different energy for all MgO-containing samples, i.e., at ∼8989 eV, and shows Cu to be predominantly present in an octahedral environment. This pre-edge feature 2 is known to progressively shift to higher energy with decreasing octahedral distortion.[55] Also in line with our results, Hilbrandt et al. noted a shift to higher energy for feature 2 for CuO/MgO compared to bulk CuO and attributed this to copper in CuO/MgO being in an octahedral or distorted octahedral geometry, occupying Mg lattice sites in a solid solution.[56]

It has been reported that electron spin resonance (ESR) measurements can distinguish between two types of copper, i.e., Cu^{2+}, in an octahedral field in the bulk of MgO and Cu^{2+} in an unclear geometry close to the surface, in such a MgO crystal lattice.[57] The nature and geometry of Cu species in our materials is expected to be further complicated, however, by the third SiO_2 component and by the magnesium silicates. EXAFS analyses nonetheless provided more insight into the geometry and bond distances of Cu present in our samples (see Table 4 and Figure S5).

Expectedly, the EXAFS data for CuO/SiO_2 and reference bulk CuO were seen to be quite similar (Table 4 and Table S1), in line with the XRD, TEM, XPS, and XANES results. A very different situation is observed for CuO/SiO_2–MgO (III), CuO/MgO(IWI)+SiO_2, and CuO/MgO (see Table 4). Importantly, no Cu–Cu contributions could be found for these samples; instead, Cu–Mg bond distances fitted for these samples are in the range 2.98–3.02 Å, i.e., similar to the Mg–Mg distance of 2.97 Å observed in periclase,[58] corroborating the presence of copper in the crystal lattice of MgO. An initial fit of the EXAFS data showed Cu to coordinate to four oxygen atoms at a bond distance of 1.92–1.94 Å (Table S2 and Figure S6), which is smaller than the Mg–O distance of ∼2.10 Å in MgO[59] and reflects the significant distortion of the crystal lattice caused by copper atom insertion; this distortion can contribute to the alteration in acid–base properties of our Cu-promoted SiO_2–MgO materials.[7] The presence of only four Cu–O contributions is not in line, however, with the UV–vis and XANES results that show Cu to be in a distorted octahedral geometry in CuO/MgO, CuO/SiO_2–MgO (III) and CuO/MgO(IWI)+SiO_2. Interestingly, Asakura et al. also observed Cu in an octahedrally distorted geometry to be present in a MgO crystal lattice to have an oxygen CN of less than six.[60] Given the strong indications for octahedral coordination, the EXAFS spectra were again analyzed with the assumption that two additional O atoms could be present. The latter fit gave results with a similar goodness-of-fit as the initial one, with two additional oxygen atoms now located at a distance of ∼2.40 Å. This corresponds very well with the average $Cu–O_{apical}$ distances of 300 (well-defined) CuO_6 complexes (Cambridge Structural Database).[61] Specifically, the structure search showed these CuO_6 coordination spheres to have a distorted octahedral geometry with bond distances in the ranges 1.88–2.00 and 2.30–2.50 Å for equatorial and apical oxygen atoms, respectively. The values obtained by EXAFS analysis of 1.94 and 2.40 Å for CuO/MgO (Table 4) can thus

Table 4. Parameters Obtained from Analysis of Cu K-Edge k^3-Weighted EXAFS of the Different Samples

sample	shell	CN[c]	r (Å)[d]	DW[e]	E_i[f]
	Cu–O	4.0	1.94	0.006	−1.0
CuO/SiO_2	Cu–O (2)	2.9	2.79	0.012	3.6
	Cu–Cu	3.2	2.86	0.012	14.2
CuO/SiO_2(IWI)+MgO[a]	Cu–O	2.8	1.93	0.005	0.9
CuO/SiO_2–MgO (III)[b]	Cu–O	4.0	1.94	0.009	4.7
	Cu–O (2)	1.5	2.48	0.149	0.3
	Cu–Mg	4.6	3.02	0.019	2.9
CuO/MgO(IWI)+SiO_2[b]	Cu–O	4.0	1.91	0.009	8.5
	Cu–O (2)	1.1	2.39	0.013	12.5
	Cu–Mg	3.7	3.00	0.016	−0.9
CuO/MgO[b]	Cu–O	4.1	1.94	0.009	7.7
	Cu–O (2)	1.5	2.40	0.013	0.1
	Cu–Mg	4.7	2.98	0.008	3.0

[a]The shells higher than the first one could not be fitted due to the presence of at least two contributions in antiphase. [b]The values for the parameters in the original fit of these samples are reported in the SI Table S2. [c]Coordination number. [d]Distance averaged over the shell. [e]Debye–Waller factor. [f]Fermi energy (edge position).

DOI: 10.1021/acscatal.5b00755
ACS Catal. 2015, 5, 6005–6015

be considered common for a Jahn−Teller distorted Cu^{2+} ion in a CuO_6 environment.

Differently from all other samples, EXAFS analysis did not find one specific element in the second Cu shell for CuO/SiO_2(IWI)+MgO due to two or more contributions in antiphase in the Fourier transform (FT). This is surprising considering that the XANES data showed features quite similar to the other samples containing both CuO and MgO. CuO/SiO_2(IWI)+MgO showed different UV−vis features and catalytic performance, though, indeed suggesting differences in Cu speciation. As EXAFS measures an average for the contribution of the various Cu species present, those present in small amounts can be difficult to discern with this technique. The EXAFS results showing most of the Cu in a solid solution with MgO thus do not exclude the presence of minor amounts of other species ($(CuO)_x$ clusters, Cu on SiO_2 or Cu present in magnesium silicates), as suggested by other techniques.

Summarizing the ex situ characterization results, it can first be noted that the TEM and XPS results indeed support the formation of surface magnesium silicates during wet-kneading. The XAS spectra show CuO/SiO_2−MgO (III), CuO/MgO-(IWI)+SiO_2, and CuO/MgO to be similar and have copper mainly present in the MgO crystal lattice sites. The solid solution formation is reflected by the distorted octahedral geometry seen for Cu^{2+}. Although the XRD and XANES data suggests that CuO/SiO_2(IWI)+MgO also can be best described as a solid solution, the UV−vis and the EXAFS data show that this material is structurally somewhat different from a copper perspective. Finally, all copper was observed to be present with oxidation state +2 only.

The results thus show that the samples prepared supporting $Cu(NO_3)_2$ on MgO or coprecipitating the nitrates of Cu and Mg have remarkably similar features, implying a similar end-state for both samples. In particular, the use of a CP method for CuO/MgO(CP)+SiO_2 might allow for the direct formation of a solid solution, which is also obtained eventually with the other sample where Cu is supported on MgO by IWI, by redistribution of Cu species either during wet-kneading or the thermal treatment. Additionally, these samples possess similar crystallinity and nature of copper species as compared with CuO/SiO_2−MgO (III), the benchmark catalyst of this study. Remarkably, the method chosen for copper addition, be it to MgO or SiO_2−MgO, then only affects the final structure to a very limited extent. On the other hand, the sample prepared by impregnating $Cu(NO_3)_2$ on SiO_2 prior to wet-kneading with MgO, i.e., CuO/SiO_2(IWI)+MgO, does show a number of structural differences such as a highly reduced crystallinity of the periclase phase, the lack of CuO subnanometric clusters and copper location and geometry.

Copper addition was furthermore shown to alter the acid−base properties of the samples (shown here for (CuO/)SiO_2−MgO (III)). The reduction in amount of acidic and strong basic sites explains the lower amounts of unwanted dehydration products that are formed. At the same time, Cu-promotion brings about a slight increase in the amount of weak basic sites, thought to be beneficial for the aldol condensation step.

2.4. Operando XAS Measurements of the Evolution in Copper Speciation. Changes in the nature of the Cu species in CuO/SiO_2−MgO (III) were studied by XAS under operando conditions following two different approaches (Figure 7). First, the effect of the chemical potential of the Lebedev process on the nature of copper was assessed under standard reaction and pretreatment conditions (experiment 1).

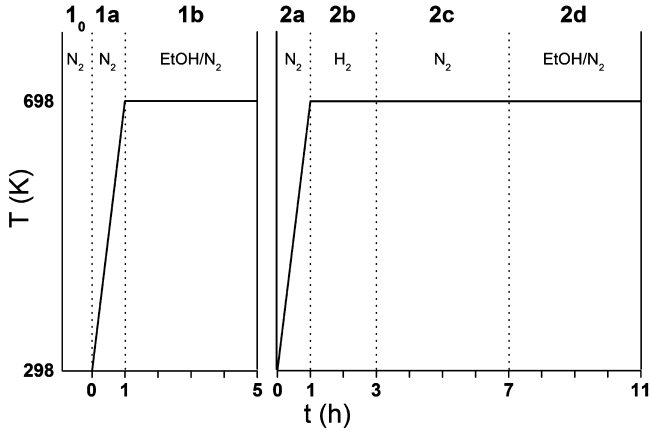

Figure 7. Graphical summary of the two experiments studying the evolution of copper in CuO/SiO_2−MgO (III) under operando conditions, including the labels of the different steps.

The capillary reactor was heated to 698 K over 1 h in N_2 flow before allowing ethanol onto the catalyst, after which XAS data was collected for 4 h time on stream. In the second experiment, the sample was prereduced by allowing pure H_2 over the catalyst for 2 h at 698 K. After reduction, the system was flushed with pure N_2 for 4 h to ensure all H_2 was removed before switching to EtOH/N_2 and again monitoring the reaction for 4 h.

To ensure operando conditions, EtOH consumption and formation of the main products were monitored by online MS. Butadiene is indeed formed, as shown by the product composition of step **1b** (Figure 8); in fact, after an initial induction period ethanol conversion, as well as butadiene and acetaldehyde yields, were all found to be stable for 4 h time on stream. The product compositions observed during steps **1b** and **2d** are in fact very similar. The slightly higher amounts seen for all compounds during experiment 2 should be interpreted with caution, as these can be due to small variations in the amount of ethanol fed or to small changes in flow as a result of packing of the catalyst bed. The time required to reach a steady state in terms of butadiene production is different for the two experiments, though, i.e., 1 h for **1b** and 3 h for **2d**.

XANES analysis provided insight into changes in Cu oxidation state during reaction. The X-ray absorption spectra, recorded over an energy range of 8965−9055 eV, were fitted with four reference samples: the spectrum of CuO/SiO_2−MgO (III) was used as reference to account for Cu species that remained unchanged; Cu foil and Cu_2O were used to assess any changes in oxidation state of Cu occurring during reaction; finally, CuO/SiO_2 was included to account for the possibility of CuO NP formation.

The fitting of the XANES recorded during all experimental steps (**1$_0$**−**1b**, **2a**−**2d**) resulted in satisfactory R-factors of <0.002. Indeed, the good match between the experimental and fitted data for experiments 1 and 2 (Figure S7) shows that the deconvolution procedure captures the chemical evolution of copper species well. The XANES obtained during step **1$_0$** (RT, nitrogen flow) should be identical to the observed for CuO/SiO_2−MgO (III) XANES measured ex situ (see above). This thus allowed us to estimate the experimental uncertainty of our fitting calculations to be ∼10% (see experimental section). As compared with step **1$_0$**, no changes are again observed in the XANES upon heating the sample under nitrogen to 698 K (step **1a**, data not shown). Only upon introduction of ethanol,

DOI: 10.1021/acscatal.5b00755
ACS Catal. 2015, 5, 6005−6015

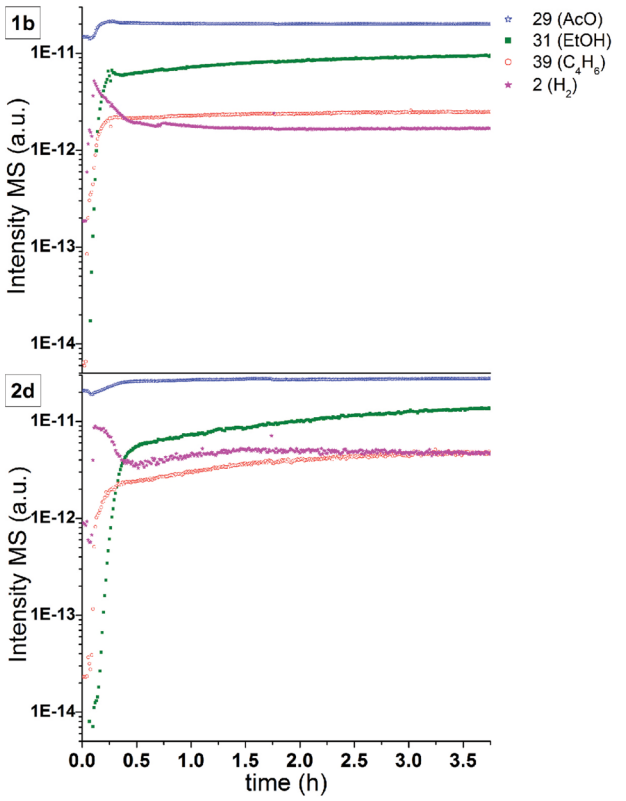

Figure 8. Online MS analysis of the product composition during operando XAS analysis of steps **1b** (top) and **2d** (bottom) as described in Figure 7.

the spectra show a remarkable change in copper speciation. In particular, the XANES data at steady state of step **1b** shows severe reduction of copper to give a composition of ~60% Cu^0, 20% Cu^+, and 20% of the Cu^{2+} species found in the initial state of CuO/SiO_2–MgO (III). It is difficult to say if the observed reduction is due to ethanol or to the H_2 formed, both being competent reductants under the applied conditions.[36] The features associated with reduced copper species appear almost instantaneously upon introduction of ethanol and the final copper composition is reached within 1 h. Importantly, no further changes are detected for the remaining 3 h time on stream.

The XAS data obtained for step **2a**, again showed the nature of Cu to be very similar to the ex situ XAS analysis and to the sample measured at 298 K (i.e., step $\mathbf{1}_0$). Indeed, the inclusion of CuO NP ($\mathbf{1}_0$) and reduced copper species (**2a**) in the fit again reflects the experimental uncertainty (~10%, see experimental section). In step **2b**, pure H_2 is allowed in the reactor and reduction of copper is observed within the first 0.5 h after which the XANES spectra do not change any more. Quantification of copper species present after prereduction (i.e., during step **2c**) again shows Cu^0 to be predominant; in fact, the fits obtained for step **2c** and **1b** are, given the experimental uncertainty, very similar (Figure 9). Finally, switching to Lebedev conditions in step **2d**, only slightly changed the composition to give ~65% Cu^0, 16% Cu^+ and 18% Cu^{2+}. This shows that the same ratio of copper oxidation states is obtained, whether the sample was subjected to a prereduction step or not.

The incomplete reduction of Cu^{2+} could be due to the presence of unreducible copper species or to slow reduction kinetics of some species with the 2 h reduction step being too short. The former is more likely, given the lack of change in the XANES spectra at the end of the reduction step **2b**. Indeed, given that the different steps taken to reach the operando conditions of **1b** and **2d** essentially give the same outcome as far as copper is concerned, it seems that a quasi-steady-state situation is reached. It is difficult to establish which of the Cu^{2+} species do not undergo reduction, but for similar systems, it has been suggested that some of the Cu^{2+} in a solid solution can retain its original oxidation state under reducing atmosphere. Although no examples could be found for copper reducibility in a $Cu_xMg_{1-x}O$ solid solution, Ni^{2+} species in $Ni_xMg_{1-x}O$ have often been observed to undergo reduction at significantly higher temperatures as compared with other Ni species.[62,63] Similarly, Cu^{2+} in a solid solution with CeO_2 was also shown to be less reducible than bulk CuO.[64,65]

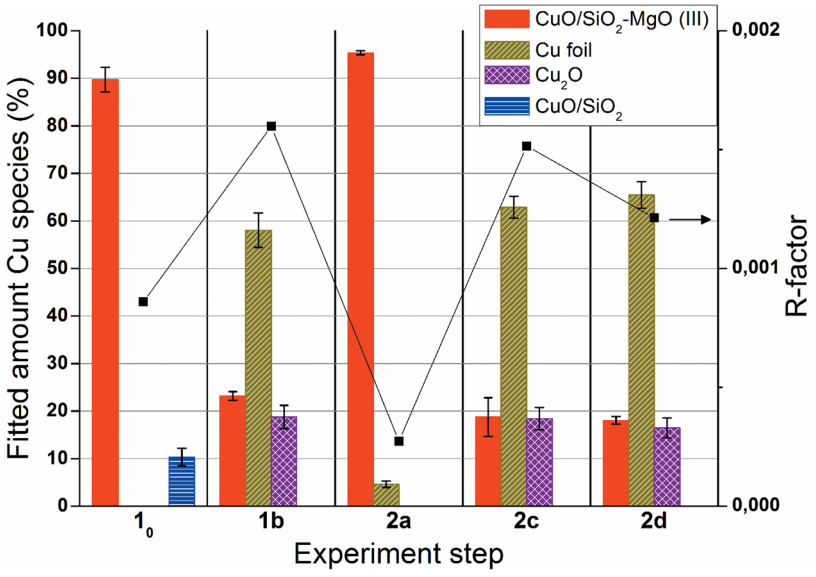

Figure 9. Amount of the different species estimated by fitting the different contributions in the XANES region and R-factor expressing the goodness-of-fit for each experimental step. Note that as steps **1a** and **2a** are identical, only the latter is included here.

DOI: 10.1021/acscatal.5b00755
ACS Catal. 2015, 5, 6005–6015

Operando EXAFS data again provided further insight into the nature of copper with regards to coordination number (CN) and nearest-neighbor contributions (Table 5 and Figure S8). For step $\mathbf{1_0}$, the Cu−O and Cu−Mg distances are, as expected, very similar to those observed for the sample analyzed ex situ, no Cu−Cu contributions are seen, and the data fits to Cu found in a distorted octahedral geometry at MgO crystal lattice sites. The EXAFS data for step **2a**, i.e., at 698 K, essentially shows the same situation, with bond distances being quite similar to $\mathbf{1_0}$, whereas CN are slightly different. For all steps, the EXAFS results are thus in good agreement with the XANES data. Notably, EXAFS shows the appearance of Cu−Cu contributions in step **1b**, with distances being similar to metallic Cu (i.e., 2.55 Å; see Table S2), thus confirming that a large percentage is now completely reduced and that Cu^0 particles are formed. As a result of Cu^0 and Cu^+ formation, the number of O and Mg atoms coordinated by Cu is lower. A similar trend is observed in **2c** and **2d**, the main difference with **1b** being the slightly lower number of O atoms coordinating to Cu.

Table 5. Parameters Obtained from Analysis of Cu K-Edge k^3-Weighted Operando EXAFS Data[a]

experiment step	shell	CN[b]	r (Å)[c]	DW[d]	E_f[e]
$\mathbf{1_0}$	Cu−O	4.4	1.94	0.009	3.5
	Cu−O (2)	2.0	2.42	0.020	−8.8
	Cu−Mg	3.7	2.87	0.015	8.8
1b	Cu−O	2.2	1.91	0.020	15.0
	Cu−Cu	3.6	2.54	0.008	−2.3
	Cu−Mg	3.3	2.91	0.002	9.5
2a	Cu−O	3.3	1.94	0.011	8.4
	Cu−O (2)	1.8	2.42	0.020	10.0
	Cu−Mg	4.0	2.92	0.020	0.5
2c	Cu−O	1.4	1.93	0.134	13.8
	Cu−Cu	3.6	2.54	0.008	−2.3
	Cu−Mg	3.3	2.91	0.003	9.5
2d	Cu−O	1.1	1.93	0.011	13.8
	Cu−Cu	3.6	2.54	0.008	−2.3
	Cu−Mg	3.3	2.91	0.002	9.5

[a]The experiment steps are shown in Figure 7. $\mathbf{1_0}$ refers to the EXAFS spectrum taken at RT prior to thermal treatment, i.e., before **1a**. [b]Coordination number. [c]Distance averaged over the shell. [d]Debye−Waller factor. [e]Fermi energy (edge position).

The EXAFS data thus also shows that in all cases (i.e., **1b**, **2c** and **2d**) a quasi-steady-state is reached in terms of Cu speciation, as indicated by same number of Cu and Mg scatterers found in the first shell, for example. While the larger amounts of Cu^0 fitted to the XANES of steps **2c** and **2d** are within the experimental error, EXAFS analysis does show a reduction in the average number of O atoms around Cu in **2c** and **2d**, thus suggesting that these might indeed be slightly more reduced than **1b**.

The time required for the measured butadiene yields to stabilize under the operando XAS conditions seems to coincide with the time required to reach a steady state in copper oxidation state. It is likely that the Cu^0 species formed are mainly responsible for the boost in butadiene yield seen upon Cu-promotion. Indeed, Iwasa and Takezawa showed ethanol dehydrogenation to occur rapidly on prereduced but not on unreduced Cu-based catalysts.[66] Similarly, Marchi et al. attributed the initial increase in activity of a Cu/SiO_2 catalyst for 2-propanol dehydrogenation to reduction of CuO to metallic Cu.[67] Finally, Carotenuto et al. used three commercial Cu-based catalysts for ethanol dehydrogenation with operando XANES,[68] proposing Cu^0 species formed in situ to be responsible for ethanol adsorption and dehydrogenation. That Cu^0 generated in situ is responsible for increased dehydrogenation activity could then also explain the similar performance reported for SiO_2−MgO Lebedev catalyst promoted with metallic Ag and CuO.[6]

We previously proposed that acetaldehyde self-condensation is rate-determining for the Cu-promoted materials,[8] whereas acetaldehyde formation itself is thought to be rate-determining for the unpromoted SiO_2−MgO catalysts.[69] This is in agreement with Makshina et al.,[6] who also observed acetaldehyde accumulation for Ag-promoted SiO_2−MgO materials and concluded that more MgO was required to perform the subsequent aldol condensation step. This shift in rate-determining step then also explains why the amount of dehydrogenation promoter introduced does not affect the overall butadiene yield for our Cu-promoted materials (in the range of 0.5−2 wt %, see ref 8), as also previously reported for Ag- and Zn-promoted ones.[6] Apparently, a small amount of promoter is already sufficient to produce more acetaldehyde than can be converted by the sites responsible for aldol condensation. While solid solution formation has been previously suggested for CuO-, ZnO-promoted SiO_2−MgO Lebedev catalysts[3] and the formation of mixed Ni, Mg silicates have been proposed, our operando results show for the first time that the oxidation state and location of Cu changes during reaction; such an in situ reduction might also occur for promoters which are chemically similar to Cu (e.g., Ni). Finally, it should be noted here that a considerable amount of copper (i.e., ∼ 40%) is present with oxidation state +1/+2, Cu species that are still expected to also contribute to the different steps of the Lebedev process. These Cu_xO species are for instance believed to poison those sites responsible for ethanol dehydration, given the significantly lower ethylene yield with promoted SiO_2−MgO materials.

Finally, the operando XAS studies shed light on the deactivation shown by the Cu-promoted catalysts during 24 h time on stream (Figure S9). UV−vis spectra of the spent CuO/SiO_2−MgO samples showed considerably more carbonaceous materials to be present on these samples than on the unpromoted catalysts (cf. Figures S10 and S11), suggesting that deactivation should be attributed to blockage of the active species. Alternatively, deactivation might be the result of sintering of the Cu^0 particles formed during reaction. Marchi et al., for instance, held sintering of metallic copper formed in situ on Cu/SiO_2 catalysts responsible for the drop seen in 2-propanol dehydrogenation activity.[67] The fact that Cu−Cu CN is the same in **1b**, **2c**, and **2d**, together with the observation that the Cu−Cu CN calculated at different times of step **2d** (not shown) does not vary during reaction, seems to exclude any sintering of Cu^0. Also taking into account that only a small amount of Cu^0 is needed to shift the rate-determining step, loss of active Cu^0 dehydrogenation sites by blockage rather than sintering is thought to be the main reason for the slight, yet gradual deactivation that is observed.

3. CONCLUSION

The higher butadiene yields obtained with Cu-promoted SiO_2−MgO catalysts are attributed to improved dehydrogenation activity and modified acid−base properties as compared with

DOI: 10.1021/acscatal.5b00755
ACS Catal. 2015, 5, 6005−6015

unpromoted SiO_2−MgO catalysts. Here, we show how different preparation methods and addition orders of Cu affect both the structure and performance of Cu-promoted SiO_2−MgO catalysts. In particular, the two materials where Cu was supported on MgO prior to wet-kneading with SiO_2 showed overall performances very similar to the benchmark catalyst (prepared by impregnation of copper on SiO_2−MgO). On the other hand, the catalyst material prepared by adding copper to SiO_2 prior to wet-kneading with MgO results in significantly worse performance. The reduced performance of the latter sample coincides with the absence of CuO subnanometric clusters, proposed to favor the aldol condensation of acetaldehyde. Extensive characterization shows all copper to be Cu^{2+} and in the MgO-containing samples, to be present in an octahedrally distorted geometry in a $Cu_xMg_{1-x}O$ solid solution. The presence of Cu^{2+} in the crystal lattice of MgO also contributes to the modification of the acid−base properties of Cu-containing SiO_2−MgO materials as compared with unpromoted ones.

Operando XAS measurements provided valuable insights into the dynamics of the copper species and on their catalytic role. In fact, the majority of Cu^{2+} is rapidly reduced to Cu^0 under reaction conditions. Furthermore, a quasi-steady-state situation in terms of ratio of Cu^0, Cu^+, and Cu^{2+} species is obtained regardless of the pretreatment history. With Cu^0 being the dominant species under reaction conditions and given the similar performance reported for Cu- and Ag-promoted SiO_2−MgO catalyst materials, it is proposed that metallic copper is in fact mainly responsible for the increased dehydrogenation activity and, as a result, the observed butadiene yields. Finally, deactivation of the copper-containing catalysts was ascribed to carbonaceous deposits on the active sites rather than to sintering of the promoter.

■ ASSOCIATED CONTENT

Supporting Information

The Supporting Information is available free of charge on the ACS Publications website at DOI: 10.1021/acscatal.5b00755.

Full experimental details; a comparison between the butadiene yield and UV−vis spectra of CuO/SiO_2−MgO (III) and SiO_2−MgO (III); the mechanism for the Lebedev process; catalytic testing of CuO/MgO and CuO/SiO_2; UV−vis spectra of CuO, CuO/MgO, and CuO/SiO_2; XPS spectra of CuO/MgO, CuO/SiO_2, and CuO/SiO_2−MgO (III); table containing the parameters calculated for the references Cu foil, Cu_2O, and CuO; additional EXAFS data; fitting of the XANES spectra obtained under operando conditions for selected steps; comparison between the butadiene yield and the UV−vis spectra (after reaction) of Cu-promoted and unpromoted SiO_2−MgO catalysts; schematic representation of the setup employed for the operando XAS measurements; comparison between the XANES spectra of SiO_2−MgO (III) promoted with 1 and 2% CuO; table containing the fragments observed with MS under operando conditions for the main products of the Lebedev process and detailed description of the experimental procedure used for the preparation of SiO_2−MgO (III) and CuO/SiO_2MgO (III) (PDF)

■ AUTHOR INFORMATION

Corresponding Authors

*(B.M.W.) E-mail: b.m.weckhuysen@uu.nl.
*(P.C.A.B.) E-mail: p.c.a.bruijnincx@uu.nl.

Notes

The authors declare no competing financial interest.

■ ACKNOWLEDGMENTS

This research has been performed within the framework of the CatchBio program. The authors gratefully acknowledge the support of the Smart Mix Program of The Netherlands Ministry of Economic Affairs and The Netherlands Ministry of Education, Culture, and Science. M.E.V. Velthoen and R. Oord are thanked for the acid−base characterization of the catalysts. The scientific staff of the DUBBLE beamline at ESRF (France) is acknowledged. S. Kalirai is thanked for his help and valuable discussions during the measurement at the DUBBLE beamline at ESRF (France).

■ REFERENCES

(1) Angelici, C.; Weckhuysen, B. M.; Bruijnincx, P. C. A. *ChemSusChem* **2013**, *6*, 1595−1614.
(2) Makshina, E. V.; Dusselier, M.; Janssens, W.; Degrève, J.; Jacobs, P. A.; Sels, B. F. *Chem. Soc. Rev.* **2014**, *43*, 7917−7953.
(3) Natta, G.; Rigamonti, R. *Chim. Ind.* **1947**, *29*, 195−201.
(4) Corson, B. B.; Jones, H. E.; Welling, C. E.; Hinckley, J. A.; Stahly, E. E. *Ind. Eng. Chem.* **1950**, *42*, 359−373.
(5) Kitayama, Y.; Satoh, M.; Kodama, T. *Catal. Lett.* **1996**, *36*, 95−97.
(6) Makshina, E. V.; Janssens, W.; Sels, B. F.; Jacobs, P. A. *Catal. Today* **2012**, *198*, 338−344.
(7) Ueda, W.; Yokoyama, T.; Moro-oka, Y.; Ikawa, T. *Chem. Lett.* **1985**, *14*, 1059−1062.
(8) Angelici, C.; Velthoen, M. E. Z.; Weckhuysen, B. M.; Bruijnincx, P. C. A. *ChemSusChem* **2014**, *7*, 2505−2515.
(9) Chary, K. V. R.; Seela, K. K.; Sagar, G. V.; Sreedhar, B. *J. Phys. Chem. B* **2004**, *108*, 658−663.
(10) Shimokawabe, M.; Takezawa, N.; Kobayashi, H. *Appl. Catal.* **1982**, *2*, 379−387.
(11) Velu, S.; Suzuki, K.; Okazaki, M.; Kapoor, M. P.; Osaki, T.; Ohashi, F. *J. Catal.* **2000**, *194*, 373−384.
(12) Praliaud, H.; Mikhailenko, S.; Chajar, Z.; Primet, M. *Appl. Catal., B* **1998**, *16*, 359−374.
(13) Wang, Z.; Wan, H.; Liu, B.; Zhao, X.; Li, X.; Zhu, H.; Xu, X.; Ji, F.; Sun, K.; Dong, L.; Chen, Y. *J. Colloid Interface Sci.* **2008**, *320*, 520−526.
(14) Kong, A.; Wang, H.; Yang, X.; Hou, Y.; Shan, Y. *Microporous Mesoporous Mater.* **2009**, *118*, 348−353.
(15) Derrien, G.; Charnay, C.; Zajac, J.; Jones, D. J.; Rozière, J. *Chem. Commun.* **2008**, 3118−3120.
(16) Bravo-Suárez, J. J.; Subramaniam, B.; Chaudhari, R. V. *J. Phys. Chem. C* **2012**, *116*, 18207−18221.
(17) Kvisle, S.; Aguero, A.; Sneeden, R. P. A. *Appl. Catal.* **1988**, *43*, 117−131.
(18) Quattlebaum, W. M.; Toussaint, W. J.; Dunn, J. T. *J. Am. Chem. Soc.* **1947**, *69*, 593−599.
(19) Prasetyanto, E. A.; Lee, S.-C.; Park, S.-E. *Bull. Korean Chem. Soc.* **2007**, *28*, 2359−2362.
(20) Munnik, P.; Wolters, M.; Gabrielsson, A.; Pollington, S. D.; Headdock, G.; Bitter, J. H.; de Jongh, P. E.; de Jong, K. P. *J. Phys. Chem. C* **2011**, *115*, 14698−14706.
(21) Gong, J.; Yue, H.; Zhao, Y.; Zhao, S.; Zhao, L.; Lv, J.; Wang, S.; Ma, X. *J. Am. Chem. Soc.* **2012**, *134*, 13922−13925.
(22) Zhu, Y.-Y.; Wang, S.-R.; Zhu, L.-J.; Ge, X.-L.; Li, X.-B.; Luo, Z.-Y. *Catal. Lett.* **2010**, *135*, 275−281.

DOI: 10.1021/acscatal.5b00755
ACS Catal. 2015, 5, 6005−6015

(23) Marella, R. K.; Neeli, C. K. P.; Kamaraju, S. R. R.; Burri, D. R. *Catal. Sci. Technol.* **2012**, *2*, 1833−1838.
(24) Shi, R.; Wang, F.; Mu, X.; Li, Y.; Huang, X.; Shen, W. *Catal. Commun.* **2009**, *11*, 306−309.
(25) Reddy, K. H. P.; Anand, N.; Venkateswarlu, V.; Rao, K. S. R.; Burri, D. R. *J. Mol. Catal. A: Chem.* **2012**, *355*, 180−185.
(26) Wang, D.; Wang, X.; Xu, R.; Li, Y. *Nanosci. Nanotechnol. Lett.* **2007**, *7*, 1−5.
(27) El-Shobaky, G. A.; Hamed, M. N.; Abdalla, F. F.; El-Molla, S. A. *Colloids Surf., A* **2002**, *207*, 293−301.
(28) Paranthaman, M.; David, K. A.; Lindemer, T. B. *Mater. Res. Bull.* **1997**, *32*, 165−173.
(29) Oku, M.; Hirokawa, K. *J. Electron Spectrosc. Relat. Phenom.* **1977**, *10*, 103−110.
(30) Grirrane, A.; Corma, A.; Garcia, H. *Chem. - Eur. J.* **2011**, *17*, 2467−2478.
(31) Raj, G. *Advanced Inorganic Chemistry Vol. II*; Krishna Prakashan Media: Uttar Pradesh, India, 2014.
(32) Claus, P.; Lucas, M.; Lücke, B.; Berndt, T.; Birke, P. *Appl. Catal., A* **1991**, *79*, 1−18.
(33) Lopez, T.; Manríquez, M. E.; Gomez, R.; Campero, A.; Llanos, M. E. *Mater. Lett.* **2000**, *46*, 21−29.
(34) Ron, H.; Rubinstein, I. *J. Am. Chem. Soc.* **1998**, *120*, 13444−13452.
(35) Rosmaninho, M. G.; Moura, F. C. C.; Souza, L. R.; Nogueira, R. K.; Gomes, G. M.; Nascimento, J. S.; Pereira, M. C.; Fabris, J. D.; Ardisson, J. D.; Nazzarro, M. S.; Sapag, K.; Araújo, M. H.; Lago, R. M. *Appl. Catal., B* **2012**, *115−116*, 45−52.
(36) Hong, Z.; Cao, Y.; Deng, J. *Mater. Lett.* **2002**, *52*, 34−38.
(37) Angelici, C. Ethanol-to-Butadiene Conversion over SiO2-MgO Catalysts: Synthesis-Structure-Performance Relationships. PhD Thesis, Utrecht University, 2015.
(38) Travert, A.; Vimont, A.; Sahibed-Dine, A.; Daturi, M.; Lavalley, J.-C. *Appl. Catal., A* **2006**, *307*, 98−107.
(39) Larina, O. V.; Kyriienko, P. I.; Soloviev, S. O. *Catal. Lett.* **2015**, *145*, 1162−1168.
(40) Angelici, C.; Velthoen, M. E. Z.; Weckhuysen, B. M.; Bruijnincx, P. C. A. *Catal. Sci. Technol.* **2015**, *5*, 2869−2879.
(41) Ono, Y.; Hattori, H. *Solid Base Catalysis*; Springer-Verlag and Tokyo Institute of Technology Press: Berlin, Heidelberg, Tokyo, 2010.
(42) Águila, G.; Gracia, F.; Cortés, J.; Araya, P. *Appl. Catal., B* **2008**, *77*, 325−338.
(43) Shimizu, K.; Maeshima, H.; Yoshida, H.; Satsuma, A.; Hattori, T. *Phys. Chem. Chem. Phys.* **2000**, *2*, 2435−2439.
(44) Velu, S.; Wang, L.; Okazaki, M.; Suzuki, K.; Tomura, S. *Microporous Mesoporous Mater.* **2002**, *54*, 113−126.
(45) Stakheev, A. Y.; Shpiro, E. S.; Apijok, J. *J. Phys. Chem.* **1993**, *97*, 5668−5672.
(46) Okada, K.; Kameshima, Y.; Yasumori, A. *J. Am. Ceram. Soc.* **1998**, *81*, 1970−1972.
(47) Bennici, S.; Gervasini, A.; Ravasio, N.; Zaccheria, F. *J. Phys. Chem. B* **2003**, *107*, 5168−5176.
(48) Sagata, K.; Imazu, N.; Yahiro, H. *Catal. Today* **2013**, *201*, 145−150.
(49) Francisco, M. S. P.; Mastelaro, V. R.; Nascente, P. A. P.; Florentino, A. O. *J. Phys. Chem. B* **2001**, *105*, 10515−10522.
(50) Ghijsen, J.; Tjeng, L. H.; van Elp, J.; Eskes, H.; Westerink, J.; Sawatzky, G. A.; Czyzyk, M. T. *Phys. Rev. B: Condens. Matter Mater. Phys.* **1988**, *38*, 11322−11330.
(51) Deka, U.; Juhin, A.; Eilertsen, E. A.; Emerich, H.; Green, M. A.; Korhonen, S. T.; Weckhuysen, B. M.; Beale, A. M. *J. Phys. Chem. C* **2012**, *116*, 4809−4818.
(52) Huang, H.-L.; Wang, H. P.; Wei, G.-T.; Sun, I.-W.; Huang, J.-F.; Yang, Y. W. *Environ. Sci. Technol.* **2006**, *40*, 4761−4764.
(53) Choy, J.; Kim, D.; Hwang, S.; Demazeau, G. *Phys. Rev. B: Condens. Matter Mater. Phys.* **1994**, *50*, 16631−16639.
(54) Acharya, A.; Behera, R.; Roy, G. S. *Lat. Am. J. Phys. Educ.* **2012**, *6*, 402−406.
(55) Lytle, F. W.; Greegor, R. B.; Panson, A. J. *Phys. Rev. B: Condens. Matter Mater. Phys.* **1988**, *37*, 1550−1563.
(56) Hilbrandt, N.; Martin, M. *J. Phys. Chem. B* **1999**, *103*, 4797−4802.
(57) Cordischi, D.; Pepe, F.; Schiavello, M. *J. Phys. Chem.* **1973**, *77*, 1240−1245.
(58) Yamaguchi, K.; Ebitani, K.; Yoshida, T.; Yoshida, H.; Kaneda, K. *J. Am. Chem. Soc.* **1999**, *121*, 4526−4527.
(59) Hazen, R. M. *Am. Mineral.* **1976**, *61*, 1280−1293.
(60) Asakura, K.; Iwasawa, K. *Mater. Chem. Phys.* **1988**, *18*, 499−512.
(61) Cambridge Structural Database. http://webcsd.ccdc.cam.ac.uk/ (accessed August 27, 2015).
(62) Hu, Y. H.; Ruckenstein, E. *Catal. Lett.* **1996**, *36*, 145−149.
(63) Ruckenstein, E.; Hu, Y. H. *Ind. Eng. Chem. Res.* **1998**, *37*, 1744−1747.
(64) Chen, J.; Zhu, J.; Chen, C.; Zhan, Y.; Cao, Y.; Lin, X.; Zheng, Q. *Catal. Lett.* **2009**, *130*, 254−260.
(65) Wang, X.; Rodriguez, A.; Hanson, J. C.; Gamarra, D.; Martínez-Arias, A.; Fernández-García, M. *J. Phys. Chem. B* **2005**, *109*, 19595−19603.
(66) Iwasa, N.; Takezawa, N. *Bull. Chem. Soc. Jpn.* **1991**, *64*, 2619−2623.
(67) Marchi, A. J.; Fierro, J. L. G.; Santamaría, J.; Monzón, A. *Appl. Catal., A* **1996**, *142*, 375−386.
(68) Carotenuto, G.; Tesser, R.; Di Serio, M.; Santacesaria, E. *Biomass Convers. Biorefin.* **2013**, *3*, 55−67.
(69) Niiyama, H.; Morii, S.; Echigoya, E. *Bull. Chem. Soc. Jpn.* **1972**, *45*, 655−659.

DOI: 10.1021/acscatal.5b00755
ACS Catal. 2015, 5, 6005−6015